ResearchGate

See discussions, stats, and author profiles for this publication at: https://www.researchgate.net/publication/263954562

Tuning Electronic Structure of Bilayer MoS2 by Vertical Electric Field: A First-Principles Investigation

ARTICLE *in* THE JOURNAL OF PHYSICAL CHEMISTRY C · SEPTEMBER 2012

Impact Factor: 4.77 · DOI: 10.1021/jp307124d

CITATIONS
73

READS
195

6 AUTHORS, INCLUDING:

Yafei Li
Nanjing Normal University
48 PUBLICATIONS **2,047** CITATIONS
SEE PROFILE

Zhongfang Chen
University of Puerto Rico at Rio Piedras
221 PUBLICATIONS **8,040** CITATIONS
SEE PROFILE

Jing Lu
Peking University
164 PUBLICATIONS **3,373** CITATIONS
SEE PROFILE

Available from: Zhongfang Chen
Retrieved on: 29 January 2016

THE JOURNAL OF PHYSICAL CHEMISTRY C

Article

pubs.acs.org/JPCC

Tuning Electronic Structure of Bilayer MoS_2 by Vertical Electric Field: A First-Principles Investigation

Qihang Liu,[†,∥] Linze Li,[‡,∥] Yafei Li,[§] Zhengxiang Gao,[†] Zhongfang Chen,*[,§] and Jing Lu*[,†]

[†]State Key Laboratory of Mesoscopic Physics and Department of Physics, Peking University, Beijing 100871, P. R. China

[‡]Department of Materials Science and Engineering, University of Michigan, Ann Arbor, Michigan 48109, United States

[§]Department of Chemistry, Institute for Functional Nanomaterials, University of Puerto Rico, San Juan 00931, Puerto Rico

Supporting Information

ABSTRACT: Interest in the two-dimensional MoS_2 material is consistently increasing because of its many potential applications, in particular in the next-generation nanoelectronic devices. By means of density functional theory computations, we systematically examined the effect of vertical electric field on the electronic structure of MoS_2 bilayer. The bandgaps of the bilayer MoS_2 monotonically decrease with an increasing vertical electric field. The critical electric fields, at which the semiconductor-to-metal transition occurs, are predicted to be in the range of 1.0−1.5 V/Å depending on different stacked conformations. Ab initio quantum transport simulations of a dual-gated bilayer MoS_2 channel clearly confirm that the vertical electric field continuously manipulates the transmission gap of bilayer MoS_2.

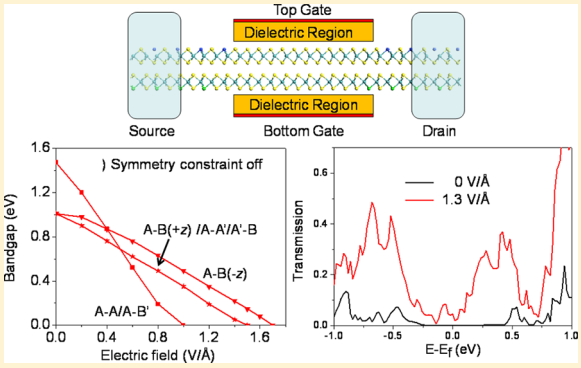

INTRODUCTION

Graphene is just the tip of the iceberg of two-dimensional (2D) nanomaterials; explorations involving the discovery of the rest of this iceberg are becoming more and more attractive.[1] Through exfoliation, layered materials with strong covalent in-plane bonds and weak van der Waals-like coupling between layers, such as transition metal dichalcogenides and transition metal oxides, can be made into single- and few-layer flakes.[1,2] With the relative fabrication easiness compared to one-dimensional materials, 2D materials are expected to have a significant impact on next-generation nanoelectronic devices. MoS_2 is a typical example of the layered transition-metal dichalcogenide family. It is composed of covalently bonded S−Mo−S sheets that are bound by weak van der Waals forces. In its bulk form, MoS_2 is a semiconductor with an indirect bandgap of 1.2 eV[3] and has attracted attentions because of its distinctive electronic, optical, catalytic, and lubricant properties.[4] The 2D MoS_2 nanostructures exhibit even more interesting properties. When the MoS_2 crystal is thinned to monolayer, a strong photoluminescence emerges, and an indirect to direct bandgap transition is thus confirmed.[5] Notably, monolayer MoS_2 transistor with room-temperature current on/off ratios of 10^8 has been achieved and demonstrates a room-temperature mobility of at least 200 $cm^2\ V^{-1}\ s^{-1}$, which is similar to that of graphene nanoribbons.[6] With such distinctive properties, 2D MoS_2 could substitute or complement graphene in many aspects.

Bandgap engineering is a powerful technique and an essential part of nanoelectronics and nanophotonics. Recent advances in engineering a graphene bandgap have motivated our study of tuning the bandgap of the technologically important 2D semiconducting MoS_2 materials. An efficient method to open a graphene bandgap is to apply a perpendicular electric field to its bilayer structure.[7] The mechanism lies in that the inversion symmetry of the bilayer graphene is broken in the presence of an external electric field; an electrostatic screening between the two layers occurs; and the π and π^* bands crossing each other at the Fermi level (E_f) are split. This method avoids the problems of fabrication complexity and reduced mobility involved in some other bandgap engineering processes such as lateral confinement and functionalization. Recently, Yue et al. studied the bandgap modulation by a transverse and perpendicular electric field in armchair MoS_2 nanoribbons ($AMoS_2NRs$) by first-principles calculations[8] and found that the bandgap of monolayer $AMoS_2NRs$ is insensitive to an external perpendicular field, but that of multilayer $AMoS_2NRs$ can be efficiently reduced by a perpendicular field. In addition, Ramasubramaniam et al. theoretically investigated the bandgap manipulation by applied electric field perpendicular to the bilayer transition-metal dichalcogenides, such as MoS_2, $MoSe_2$, $MoTe_2$, and WS_2, and by imposing symmetry constraints, they predicted that the critical electric fields, at which the bilayer structures transform from semiconductor to metal, are between 0.2−0.3 V/Å.[9]

However, MoS_2 bilayers have five different stacking patterns, which cause different interlayer distance, stability, and bandgap,

Received: July 18, 2012
Revised: September 10, 2012
Published: September 17, 2012

 © 2012 American Chemical Society dx.doi.org/10.1021/jp307124d | J. Phys. Chem. C 2012, 116, 21556−21562

thus a systematic study over all the conformations is necessary. In addition, when an unreasonable symmetry constraint is imposed in the band structure calculations under finite vertical electric field for a structure with z-symmetry, an artificial dependence of the bandgap on the electric field may emerge, and the critical field for the semiconducting-to-metallic transition is usually underestimated. Therefore, more reliable results are expected after considering the symmetry breaking for the z-symmetrical conformations under the applied field.

In this article, by means of density functional theory (DFT) computations and non-equilibrium Green's function (NEGF) method, we reveal that bandgaps of the bilayer MoS_2 with different stacking patterns all decrease monotonically with increasing the electric field perpendicular to the layers, and finally, the systems turn to metallic. The more reliable critical electric fields (in the range of 1.0−1.5 V/Å depending on the stacked conformations) are obtained. The difference from the previous results is mainly because the inversion symmetry breaking under the electric field is taken into account in our calculations. Subsequently, we provide a quantum transport simulation of a dual-gated bilayer MoS_2 device and confirm that the zero transmission gaps (ZTG) also decrease with the applied electric field. Our work is expected to stimulate the applications of such few-layered transition-metal dichalcogenides in nanoelectronics and nanophotonics.

MODEL AND METHODS

A supercell model is built. We use the lattice parameter $a = b = 3.16$ Å according to experimental value.[10] The geometry optimization and electronic properties are calculated by using DFT implemented in the Dmol^3 package.[11] To treat the long-range dispersion, two schemes are used: one is the local density approximation (LDA) to the exchange-correlation functional. In the minimum energy configuration, the charge clouds overlap, and it turns out that the LDA tends to overestimate attractions.[12] The other scheme is the generalized gradient approximation to the exchange-correlation functional of Perdew, Burke, and Ernzerhof (PBE) form,[13] with the inclusion of dispersion correction (PBE+D) proposed by Ortmann, Bechstedt, and Schmidt.[14] The Dmol^3 code has been extended to include the static potentials arising from an externally applied electric field. The electric field can be featured as an additional sawtooth potential along the z direction with discontinuity at the mid plane of the vacuum region of the supercell. We place the subject structures in the bottom part of the supercell, and our supercells are large enough (35 Å) to ensure that the discontinuity of the sawtooth potential as well as the interaction with spurious replicas along the z direction can be safely avoided. The double numerical basis set plus polarization (DNP) is employed, and the first Brillouin zone is sampled on a $24 \times 24 \times 1$ k-point Monkhorst−Pack mesh[15] for the density optimizations. The geometries are optimized under zero electric field and kept fixed hereafter since the influence of the band structure caused by the geometry disturbance is negligible. The automatic symmetry constraint is switched off, and the effects of the imposition of symmetry constraint will be discussed later.

A two-probe bilayer MoS_2 model with dual gate is fabricated to simulate the transport properties. Different from a single-gated transportation model, a dual-gated device can control not only the doping level but also the vertical electric field applied to the channel. Electron transport properties are calculated by the DFT coupled with NGEF formalism implemented in the ATK 11.8 package.[16] Single-ζ plus polarization (SZP) basis sets are employed. The k-points of the electrodes and central region, which are generated by the Monkhorst−Pack scheme as well, are set to $1 \times 50 \times 50$ and $1 \times 50 \times 1$, respectively. We used LDA for the exchange-correlation functional. A dual-gated bilayer MoS_2 channel with SiO_2 dielectric buffer layers is considered.[17] The effect of the gate voltages is calculated by solving the Poisson equation self-consistently, instead of simply shifting the central region's chemical potential. The temperature is set to 300 K. The system is divided into three parts: left electrode, scattering region (SR), and right electrode. The transmission spectrum can be calculated from the Green's function approach:

$$T(E) = Tr[t^{\dagger}t] = Tr[\Gamma_L G^r \Gamma_R G^{r\dagger}] \quad (1)$$

Here, t is the transmission matrix, and G^r and $\Gamma_{L(R)}$ represent the retarded Green's function in the SR and coupling matrix between the left (right) electrode and the SR:

$$G^r = (ES - H - \Sigma_L - \Sigma_R)^{-1} \quad (2)$$

$$\Gamma_{L(R)} = i(\Sigma_{L(R)} - \Sigma_{L(R)}^{\dagger}) \quad (3)$$

where $\Sigma_{L(R)}$ is the corresponding self-energy term.

RESULTS AND DISCUSSION

Geometries, Stabilities, and Band Structures of MoS_2 Bilayers with Different Stacking Patterns under Zero Electric Field. We first present our results of the MoS_2 monolayer. The band structures of the MoS_2 monolayer are shown in Figure S1, Supporting Information. A direct bandgap is located at the K point, and the 1.80 eV bandgap value is in agreement with the experimental data (about 1.8 eV)[5b] and previous LDA results (1.87 eV).[18] When the MoS_2 monolayer is applied with an external perpendicular electric field of even up to $E_{\perp} = 2.0$ V/Å, its bandgap is almost unchanged.

With different stacking conformations, two MoS_2 monolayers can form five different bilayer structures (Figure 1). Note that, in each MoS_2 monolayer, every S atom in the upper S sublayer is right on top of one S atom in the lower S sublayer; thus, we represent one pair of S atoms by one yellow circle for a concise scheme. In this work, we refer to the different bilayer structures by the notation introduced in Figure 1. In the A-A and A-A′ conformation (Figure 1a,b), two monolayers are aligned. Their difference lies in that atoms of the same type are superimposed in the A-A case, while one type of atom is on top of the other type in the A-A′ case, which is the most studied in the previous calculations.[9,10] In the A′-B conformation (Figure 1c), the Mo atoms are superimposed, and the S atoms in the top monolayer are above the hexagon centers of the bottom monolayer; in the A-B′ conformation (Figure 1d), the S atoms are superimposed, and the Mo atoms in the top monolayer are above the hexagon centers of the bottom monolayer; and in the A-B conformation (Figure 1e), the S atoms of the top monolayer are superimposed on the Mo atoms of the bottom monolayer, and the Mo atoms of the top monolayer are above the hexagon centers of the bottom monolayer. We also provide a perspective view of the optimized A-B stacked bilayer MoS_2 in Figure 1f.

The interlayer distances, relative energies, and binding energy based on the LDA and PBE-D functional of the five different bilayer structures are given in Table 1. According to LDA computations, the five bilayer configurations can be divided into two categories: the first has much longer interlayer

dx.doi.org/10.1021/jp307124d | J. Phys. Chem. C 2012, 116, 21556−21562

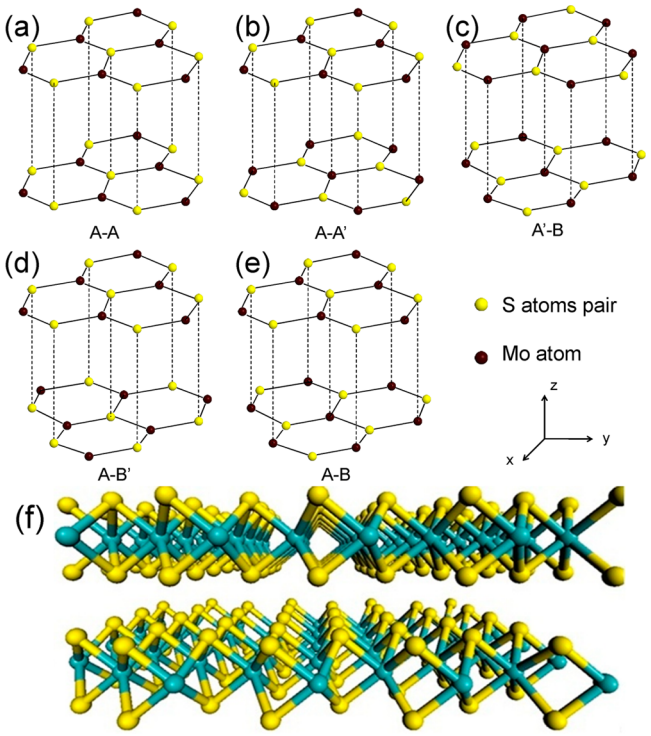

Figure 1. (a–e) Drawing schemes of five bilayer MoS_2 structures. We represent one pair of S atoms by one yellow circle for a concise scheme. (f) Perspective view of the optimized A-B stacked bilayer MoS_2.

Table 1. Interlayer Distances (d), Relative Energies (ΔE), Binding Energies (E_b), Energy Level Splitting at the Γ Point of the Valence Band (E_s), and Bandgaps (E_g) of Five Different MoS_2 Bilayer Structures Based on the LDA and PBE-D Methods

structure		A-B	A-A′	A′-B	A-B′	A-A
d (Å)	LDA	5.93	5.99[a]	5.98	6.66	6.71
	PBE-D	6.24	6.27	6.33	6.82	6.83
ΔE (meV)	LDA	0	0.3	4.0	13.8	14.5
	PBE-D	0.6	0	2.9	11.8	12.2
E_b (meV)	LDA	26.2	25.9	22.2	12.4	11.7
	PBE-D	33.6	34.1	31.3	22.3	21.9
E_g (eV)	LDA	1.01	1.09	1.06	1.47	1.47
E_s (eV)	LDA	0.94	0.85	0.90	0.52	0.49

[a]Experimental value: 6.14 Å.[19]

distances and consists of A-B′ (6.66 Å) and A-A (6.71 Å), and the second has three configurations with shorter interlayer distances, namely, A-B (5.93 Å), A-A′ (5.99 Å), and A′-B (5.98 Å). The larger interlayer distance in the A-B′ (6.66 Å) and A-A (6.71 Å) conformations is attributed to the stronger repulsion arising from the S atoms superimposing in the two conformations. These structural features highly correlate their relative stabilities. The lowest-energy conformation is the A-B stacking, closely followed by the A-A′ conformation (only 0.3 meV per atom higher in energy), which is the most reported conformation for bulk MoS_2. The energy of the A′-B conformation is slightly higher than those of the A-B and A-A′ conformations by about 4 meV/atom. Because of the stronger repulsion caused by the superimposed S atoms, the A-B′ and A-A conformations are 9.8–14.5 meV/atom higher in energy than the A-B, A-A′, and A′-B conformations. In the A-B and A-A′ conformations, different types of atoms are superimposed and thus generate more attractive potential, which leads to a lower energy. The calculated interlayer distance of the A-A′ conformations at the LDA level is merely 0.15 Å smaller than the experimental value of 6.14 Å for bulk MoS_2.[19]

The PBE-D results also divide the five conformations into two similar categories: one with larger interlayer distance and higher relative energy, including A-B′ (6.82 Å) and A-A (6.83 Å), and the other with smaller interlayer distance and lower relative energy, including A-B (6.24 Å), A-A′ (6.27 Å), and A′-B (6.33 Å). The interlayer distances given by PBE-D are about 0.2 Å larger than their respective LDA values. The interlayer distance of the A-A′ conformation at the PBE-D level is 0.13 Å larger than the experimental value of bulk MoS_2.[19] Therefore, the experimental interlayer distance (6.14 Å) for the A-A′ conformation is roughly an average over the LDA (5.99 Å) and PBE-D (6.27 Å) values. The relative stability of the five conformations is similar to the LDA result except that the A-A′ conformation is 0.5 meV per atom lower in energy than that of A-B conformation in the PBE-D calculations. Though in the actual MoS_2 bulk, the A-A′ conformation is observed,[19] other conformations probably exist in bilayer MoS_2. The binding energies based on the PBE-D level are among 20–35 meV, which are about 10 meV larger than their LDA counterparts. In light of the small difference between the LDA and PBE-D geometry and stability, in the electronic structure and transport calculations, we adopt the LDA method, and the discussions are based on the LDA optimized geometry unless otherwise mentioned.

Unlike the MoS_2 monolayer with a direct bandgap at the K point, the five conformations of MoS_2 bilayers all have indirect bandgaps. We choose the A-A and A-A′ conformations as the representative for the category with a larger and smaller interlayer distance, respectively, to explore the relationship between the interlayer distance and the corresponding bandgap. Figure 2a shows the band structures of the A-A and A-A′ bilayer conformations under zero electric field. In both cases, the direct bandgap at the K point remains to be 1.80 eV, while the Γ point energy level of the valence band becomes higher than the K point of the valence band. Since the indirect bandgap of the bilayer MoS_2 is determined by the K point energy level of the conduction band and the Γ point energy level of the valence band, we now analyze the states at these two points.

The states at the K point of the conduction band are primarily composed of the strongly localized d orbitals at the Mo atom sites, and the double degeneracy at the K point of the conduction band is nearly intact in MoS_2 bilayer due to the very weak interaction between them. However, the states of the valence band at the Γ point are mainly contributed by the outer p orbitals of the S atom sites and the internal d orbitals of the Mo atom sites. The stronger interaction between the outer p orbitals of the valence band at the Γ point belonging to different MoS_2 layers lifts their double level degeneracy. The uplifted energy level at the Γ point of the valence band is even higher than that at the K point of the valence band, and thus, a direct to indirect bandgap transition occurs.

A smaller interlayer distance implies a stronger interlayer coupling interaction (Figure 2c), a larger energy level splitting at the Γ point of the valence band (0.49 eV for the A-A conformation and 0.85 eV for the A-A′ conformation), and eventually a smaller band gap. Therefore, the structures with

dx.doi.org/10.1021/jp307124d | J. Phys. Chem. C 2012, 116, 21556–21562

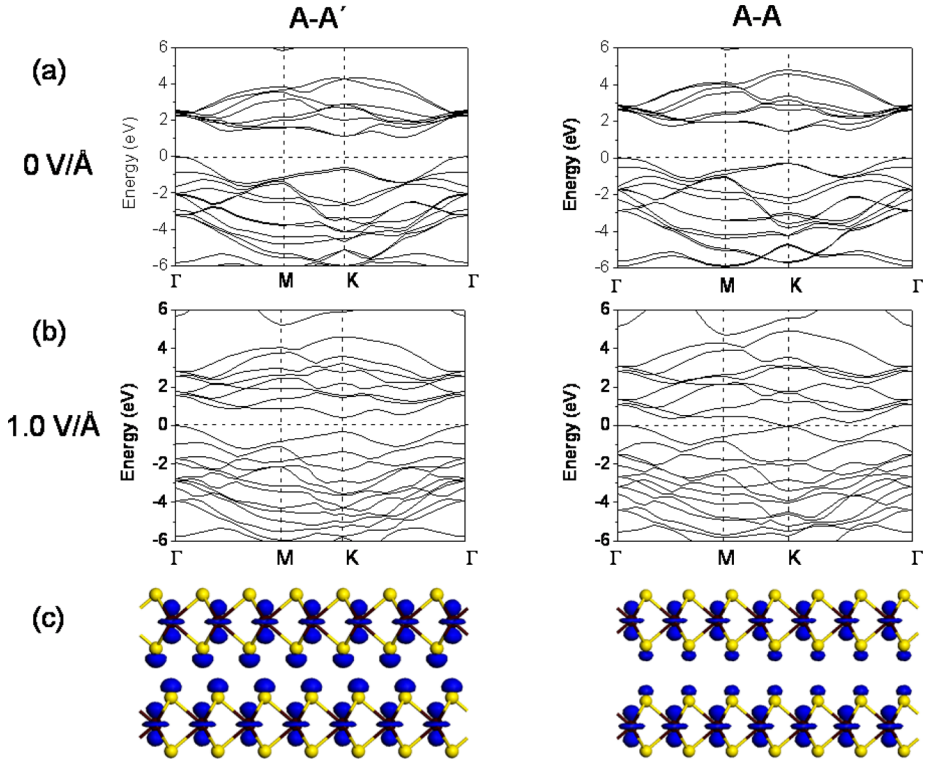

Figure 2. (a,b) Band structures under $E_\perp$ = 0 (a) and 1.0 V/Å (b) of the A-A′ and A-A MoS_2 bilayer conformations. (c) Electron density (isovalue, 0.1 au) at the Γ point of the valence band under $E_\perp$ = 0 V/Å. The valence band top is set to zero. Yellow balls represent S atoms.

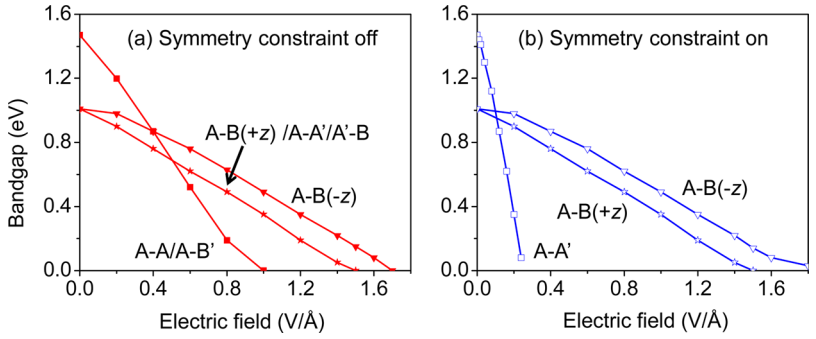

Figure 3. Bandgap of the bilayer MoS_2 as a function of applied electric field along $+z$ and $-z$ directions with the symmetry constraint off (a) and on (b). For all the conformations except the A-B one, applying electric field along $+z$ direction and $-z$ directions have the same effect.

smaller interlayer distances have smaller bandgaps. This trend holds true also for other bilayer configurations (Table 1).

Effect of External Electric Field to the Band Gaps of MoS_2 Bilayers. Previous studies suggest that a bandgap can be opened by a perpendicular applied electric field in bilayer or few-layer graphene; the gap collapses, and the system turns back to metallic when the electric field is further increased.[20] Will the external electric field also reduce the band gap of MoS_2 bilayers?

The answer is yes. In Figure 2a, we present the band structures of the A-A′ and A-A conformations of MoS_2 bilayer under $E_\perp$ = 1.0 V/Å. The bandgap of the A-A′ conformation reduces to 0.4 eV; while the A-A conformation has become metallic from semiconducting. Actually, the bandgaps of all five MoS_2 bilayer structures decrease monotonically with the increasing electric field strength, as shown in Figure 3a. Similar to the case for interlayer distances (or band gaps), the bandgap versus electric field relationship can also be divided into two groups, A-B′ pairs up with A-A to form the first group, they have indistinguishable curves; in the second group, the curves for A-A′ and A′-B are almost identical with that of the A-B ($+z$ direction) conformation.

Interestingly, applying $E_\perp$ along $+z$ direction and $-z$ directions has different effects on the band gap of A-B layer, while it has the same effect on the other four configurations. This is because only in the A-B bilayer does the spontaneous polarization exist. When applying $E_\perp$ on the A-B conformation along the $+z$ direction, its bandgap decreases almost linearly to the field strength, while applying the $-z$ direction $E_\perp$ results in a nonlinear modulation on the bandgap. The critical fields are estimated to be 1.5 V/Å and 1.7 V/Å for the $+z$ and $-z$ direction field, respectively. Under a $-z$ direction field below the threshold 0.2 V/Å, the bandgap of this system is almost unchanged. This threshold electric field could be caused by a spontaneous polarization existing between the two monolayers. Under zero bias, each Mo atom has 0.4e positive charge and S atom has 0.2e negative charge in terms of Mullikan analysis. The S atoms of the top monolayer and the Mo atoms of the

dx.doi.org/10.1021/jp307124d | J. Phys. Chem. C 2012, 116, 21556−21562

bottom monolayer are superimposed, while the Mo atoms of the top monolayer and the S atoms of the bottom monolayer are not, so there exists a spontaneous polarization along the $+z$ direction. Thus, the bandgap of the A-B bilayer can only be increased by a $-z$ direction electric field large enough to overcome the intrinsic electric polarization.

The bandgap modulation discussed above arises from the well-known Stark effect, which has been observed in the previous studies on BN and MoS_2 sheets and armchair nanoribbons.[8,9,21] External perpendicular electric field induces a potential difference between the two layers. As a result, the energy bands belonging to different MoS_2 layers are separated from each other entirely. The potential difference U can be expressed approximately by $U = -dE^*e$, where E^* is the screened electric field (external field plus that caused by charge redistribution) and d is the interlayer distance. In MoS_2 bilayer, the stronger the electric field is, the larger the band splitting is, and thus the smaller the band gap. However, the Stark effects do not always reduce the band gap of a system. For example, there is a linear Stark effect in the zigzag BN nanoribbons (ZBNNRs), and the mechanism arises from the spontaneous electric polarization existing in ZBNNRs.[21b] The conducting electrons and holes in this system are localized separately at the B and N edges, respectively; thus, there is a strong intrinsic electric field even when no external field is applied. Applied fields along different directions enhance or weaken the equivalent field, and thus, the bandgap increases or decreases due to the Stark effect. In our case, only the A-B conformation has the intrinsic symmetry broken and has slight spontaneous polarization, as discussed before. Therefore, the Stark effect leads to the bandgap reduction in the other four conformations, while the bandgap of the A-B conformation is almost unchanged below the threshold 0.2 V/Å along the $-z$ direction.

Compared with the A-B, A-A′, and A′-B conformations, the A-A and A-B′ conformations have larger interlayer distances. As a result, the potential differences in these two conformations are larger and so are the band splitting. Larger band splittings result in a quicker decreasing of the bandgap. Therefore, the critical fields for the A-A and A-B′ conformations with larger interlayer distances are smaller. In fact, the critical field for the A-A and A-B′ conformations are both 1.0 V/Å; while the critical field for the A-B ($+z$ direction), A-A′, and A′-B conformations are all 1.5 V/Å.

The absence of the inversion symmetry along the z direction in the A-B conformation of MoS_2 bilayer leads to the spontaneous polarization and the bandgap dependence on the direction of $E_\perp$. However, though the other four configurations have z-symmetry under zero electric field, their z-symmetry will be destroyed by the external electric field. If an unreasonable symmetry constraint is imposed in the band structure calculations under finite vertical electric field for a structure with z-symmetry, an artificial dependence of the bandgap on the electrical field will be led to. We provide the calculated band gap of bilayer graphene as a function of the vertical electric field with and without imposition of symmetry constraint and compare them with the experimental values in Figure S2, Supporting Information. The theoretical curve without imposition of symmetry constraint is consistent with the experiment, while the theoretical bandgap with imposition of symmetry constraint is too sensitive to the vertical electric field. On the basis of the physical picture and the comparison with the experimental values, we can conclude that the band gap values without imposition of symmetry constraint are more reliable than those with imposition of symmetry constraint. In MoS_2 bilayer structures, when the symmetry constraint is switched on, the response of the bandgap of the A-A′ conformation to $E_\perp$ also become much more sensitive, and the critical field greatly reduces from 1.5 to 0.26 V/Å (Figure 3). The latter artificial value is consistent with the recent calculations of Ramasubramaniam et al., suggestive of imposition of symmetry constraint therein.[9] Because the A-B conformation has no z-symmetry under zero electric field, whether the symmetry constraint is used does not change the E_g–$E_\perp$ relationship at all.

Quantum Transport Simulation of a Dual-Gated A-A′ Bilayer MoS_2 Structure. The modulation of the bandgap by vertical electric field in the bilayer MoS_2 should be reflected in the transport properties. Here, we perform first-principles quantum transport simulation of a dual-gated A-A′ bilayer MoS_2 structure as shown in Figure 4a.

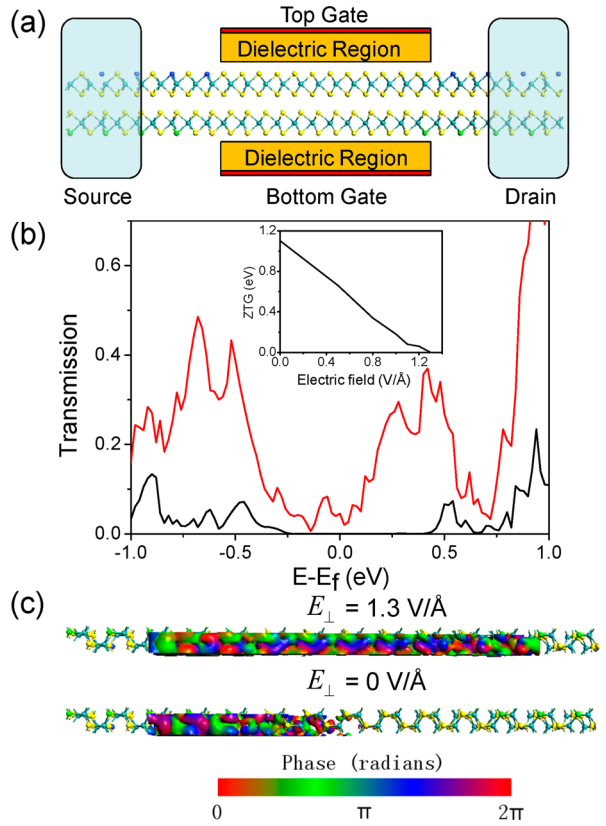

Figure 4. Dual-gated field effect transistor based on the A-A′ MoS_2 bilayer comformation. (a) Schematic model. The channel is 4.9 nm long, and the electrodes are composed of doping homogeneous bilayer MoS_2. Dark green ball, Mo; yellow ball, S; blue ball, N; light green ball, Cl. (b) Transmission spectrum under $E_\perp$ = 0 V/Å (black line) and 1.3 V/Å (red line). Inset: ZTG as a function of the applied electric field. (c) Transmission eigenstates at E_f and at the (0,0) point of the k-space under $E_\perp$ = 0 V/Å and 1.3 V/Å. The isovalue is 0.1 au.

In the experiments, the MoS_2 monolayer channel is connected to metal leads (like Au) that serve as source and drain electrodes.[6] However, we cannot apply vertical electric field on the electrode regions in the model. As a result, the metal leads here only provide an electron doping, causing E_f of contacted bilayer MoS_2 to shift, and the states remain absent in the band gap of bilayer MoS_2 contacted with metal, which results in the failure of the observation of decrease of ZTG with

dx.doi.org/10.1021/jp307124d | J. Phys. Chem. C 2012, 116, 21556–21562

the increasing electric field. In addition, the bonding between the metal and S atoms and the resulting contact resistance are complicated.[22] In order to observe the decrease of ZTG with increasing electric field and avoid the complex interaction between the metal electrode and bilayer MoS_2, we generate the electrodes by doping homogeneous bilayer MoS_2. In the uppermost and lowest sulfur layers, a nitrogen and a chlorine atom substitute every other sulfur atom, respectively, so that the E_f of the lead region is close to that of the pristine bilayer MoS_2 (the middle point of the band gap). The top gate and bottom gate voltages are defined as V_t and V_b. The distance between the two gates is d_0 = 41 Å in our model, and the thickness of the two identical dielectric regions is d_i = 13 Å. The dielectric constant of the dielectric region is ε = 3.9, which models SiO_2. The length of the gated-channel is 4.9 nm. The vertical electric field and corresponding total doping level applied to the device are obtained as follows:[17]

$$E_\perp = \frac{V_b - V_t}{(d_0 - 2d_i) + 2d_i/\varepsilon} \quad (4)$$

$$V_g = V_b + V_t \quad (5)$$

where the total doping and bias voltage are both set to zero.

The transmission spectra of the A-A′ bilayer MoS_2 under a vertical electric field of $E_\perp$ = 0 and 1.3 V/Å (Figure 4b). Under no electric field, the width of the ZTG region is 1.10 eV, which coincides with the corresponding DFT bandgap (1.09 eV). When the electric field is applied, both edges of ZTG move toward E_f, and the gap decreases linearly with the applied field except in the vicinity of the critical field (see the inset of Figure 4b). The ZTG vanishes, and the whole device becomes metallic at $E_\perp$ = 1.3 V/Å, in agreement with the band calculation (1.5 V/Å) without imposition of symmetry constraint. This agreement once confirms the necessity of canceling the symmetry constraint in the band calculation for the *z*-symmetrical conformations.

The difference between the semiconducting and metallic state is also illustrated by the transmission eigenchannels at E_f and at the (0,0) point of the *k*-space (Figure 4c). The transmission eigenvalue without $E_\perp$ is 1.95×10^{-7}, and the incoming wave function is almost completely scattered, so that it is unable to reach the other lead. In sharp contrast, the transmission eigenvalue at $E_\perp$ = 1.3 V/Å is 0.33; the incoming wave function is less scattered; and far more of the incoming wave is able to reach the other lead.

CONCLUSIONS

In summary, by means of DFT computations, we have demonstrated that the vertical electric field can continuously tune the electronic structure of MoS_2 bilayers. The bandgaps of the two-dimensional structures decrease monotonically with increasing electric bias and fall to zero eventually when the electric field is in the range of 1.0−1.5 V/Å, depending on the bilayer stacking patterns. After considering the inversion symmetry breaking under the electric field, the critical field is 4−5 times larger than that reported in the previous calculations. The effects of the vertical electric field are also verified by the ab initio quantum transport simulation of a dual-gated bilayer MoS_2 device. A sizable transmission gap, which is comparable with the bandgap, and its monotonic decrease with the electric field are observed. Our work is expected to promote the applications of such few-layered transition-metal dichalcogenides in the next-generation nanoelectronic devices.

ASSOCIATED CONTENT

Supporting Information

Band structures of the monolayer MoS_2 under a vertical electric field of 0 and 2.0 V/Å; comparison of the calculated (with the symmetry constraint switched on and off) and observed bandgap of the bilayer graphene as a function of applied vertical electric field. This material is available free of charge via the Internet at http://pubs.acs.org.

AUTHOR INFORMATION

Corresponding Author

*E-mail: jinglu@pku.edu.cn (J.L.); zhongfangchen@gmail.com (Z.C.).

Author Contributions

‖These authors contributed equally to this work.

Notes

The authors declare no competing financial interest.

ACKNOWLEDGMENTS

This work was supported in China by the NSFC (Grant Nos. 90206048, 20771010, 10774003, 90606023, 11274016, and 20731160012), National 973 Projects (Nos. 2006CB932701, 2007AA03Z311, and 2007CB936200, 2013CB932604 MOST of China), Fundamental Research Funds for the Central Universities, National Foundation for Fostering Talents of Basic Science (No. J1030310/No.J1103205), Program for New Century Excellent Talents in University of MOE of China, and in USA by Department of Defense (Grant W911NF-12-1-0083) and partially by NSF (Grant EPS-1010094).

REFERENCES

(1) For selected recent reviews, see (a) Osada, M.; Sasaki, T. *J. Mater. Chem.* **2009**, *19*, 2503−2511. (b) Golberg, D.; Bando, Y.; Huang, Y.; Terao, T.; Mitome, M.; Tang, C.; Zhi, C. *ACS Nano* **2010**, *4*, 2979. (c) Mas-Ballesté, R.; Gómez-Navarro, C.; Gómez-Herrero, J.; Zamora, F. *Nanoscale* **2011**, *3*, 20−30. (d) Rao, C. N. R.; Ramakrishna Matte, H. S. S.; Subrahmanyam, K. S. *Acc. Chem. Res.* **2012**, DOI: 10.1021/ar300033m.

(2) For example, (a) Novoselov, K. S.; Jiang, D.; Schedin, F.; Booth, T. J.; Khotkevich, V. V.; Morozov, S. V.; Geim, A. K. *Proc. Natl. Acad. Sci.* **2005**, *102*, 10451. (b) Coleman, J. N.; Lotya, M.; Neil, A. O.; Bergin, S. D.; King, P. J.; Khan, U.; Young, K.; Gaucher, A.; De, S.; Smith, R. J.; et al. *Science* **2011**, *331*, 568. (c) Lin, Y.; Williams, T. V.; Xu, T. B.; Cao, W.; Elsayed-Ali, H. E.; Connell, J. W. *J. Phys. Chem. C* **2011**, *115*, 2679.

(3) Kam, K. K.; Parkinson, B. A. *J. Phys. Chem.* **1982**, *86*, 463.

(4) (a) Gourmelon, E.; Lignier, O.; Hadouda, H.; Couturier, G.; Bernede, J. C.; Tedd, J.; Pouzet, J.; Salardenne, J. *Sol. Energy Mater. Sol. Cells* **1997**, *46*, 115. (b) Ho, W. K.; Yu, J. C.; Lin, J.; Yu, J. G.; Li, P. S. *Langmuir* **2004**, *20*, 5865. (c) Bernede, J. C.; Pouzet, J.; Gourmelon, E.; Hadouda, H. *Synth. Met.* **1999**, *99*, 45. (d) Muratore, C.; Voevodin, A. A. *Surf. Coat. Technol.* **2006**, *201*, 4125. (e) Kim, Y.; Huang, J. L.; Lieber, C. M. *Appl. Phys. Lett.* **1991**, *59*, 3404.

(5) (a) Splendiani, A.; Sun, L.; Zhang, Y. B.; Li, T. S.; Kim, J.; Chim, C. Y.; Galli, G.; Wang, F. *Nano Lett.* **2010**, *10*, 1271. (b) Mak, K. F.; Lee, C.; Hone, J.; Shan, J.; Heinz, T. F. *Phys. Rev. Lett.* **2010**, *105*, 136805.

(6) Radisavljevic, B.; Radenovic, A.; Brivio, J.; Giacometti, V.; Kis, A. *Nat. Nanotechnol.* **2010**, *6*, 147.

(7) (a) Yu, E. K.; Stewart, D. A.; Tiwari, S. *Phys. Rev. B* **2008**, *77*, 195406. (b) McCann, E. *Phys. Rev. B* **2006**, *74*, 161403. (c) Min, H. K.; Sahu, B.; Banerjee, S. K.; MacDonald, A. H. *Phys. Rev. B* **2007**, *75*,

155115. (d) Castro, E. V.; Novoselov, K. S.; Morozov, S. V.; Peres, N. M. R.; Dos Santos, J. M. B. L.; Nilsson, J.; Guinea, F.; Geim, A. K.; Neto, A. H. C. *Phys. Rev. Lett.* **2007**, *99*, 216902. (e) Castro, E. V.; Novoselov, K. S.; Morozov, S. V.; Peres, N. M. R.; Dos Santos, J. M. B. L.; Nilsson, J.; Guinea, F.; Geim, A. K.; Neto, A. H. C. *J. Phys.: Condens. Matter* **2010**, *22*, 175503.
(8) Yue, Q.; Chang, S.; Kang, J.; Zhang, X.; Shao, Z.; Qin, S.; Li, J. *J. Phys.: Condens. Matter* **2012**, *24*, 335501.
(9) Ramasubramaniam, A.; Naveh, D.; Towe, E. *Phys. Rev. B* **2011**, *84*, 205325.
(10) Boker, T.; Severin, R.; Muller, A.; Janowitz, C.; Manzke, R.; Voss, D.; Kruger, P.; Mazur, A.; Pollmann. *J. Phys. Rev. B* **2011**, *64*, 235305.
(11) Delley, B. *J. Chem. Phys.* **1990**, *92*, 508.
(12) Meijer, E. J.; Sprik, M. *J. Chem. Phys.* **1996**, *105*, 8684.
(13) Perdew, J. P.; Burke, K.; Ernzerhof, M. *Phys. Rev. Lett.* **1996**, *77*, 3865.
(14) Ortmann, F.; Bechstedt, F.; Schmidt, W. G. *Phys. Rev. B* **2006**, *73*, 205101.
(15) Monkhorst, H. J.; Pack, J. D. *Phys. Rev. B* **1976**, *13*, 5188.
(16) (a) ATOMISTIX Toolkit and D. Copenhagen, 2011; http://www.quantumwise.com. (b) Brandbyge, M.; Mozos, J. L.; Ordejon, P.; Taylor, J.; Stokbro, K. *Phys. Rev. B* **2002**, *65*, 165401. (c) Taylor, J.; Guo, H.; Wang, J. *Phys. Rev. B* **2001**, *63*, 245407.
(17) Ni, Z. Y.; Liu, Q. H.; Tang, K. C.; Zheng, J. X.; Zhou, J.; Qin, R.; Gao, Z. X.; Yu, D. P.; Lu, J. *Nano Lett.* **2011**, *12*, 113.
(18) Ataca, C.; Sahin, H.; Akturk, E.; Ciraci, S. *J. Phys. Chem. C* **2011**, *115*, 3934.
(19) Mathur, H.; Baranger, H. U. *Phys. Rev. B* **2001**, *64*, 235325.
(20) (a) Zhang, Y. B.; Tang, T. T.; Girit, C.; Hao, Z.; Martin, M. C.; Zettl, A.; Crommie, M. F.; Shen, Y. R.; Wang, F. *Nature* **2009**, *459*, 820. (b) Tang, K.; Qin, R.; Zhou, J.; Qu, H.; Zheng, J.; Fei, R.; Li, H.; Zheng, Q.; Gao, Z.; Lu, J. *J. Phys. Chem. C* **2011**, *115*, 9458.
(21) (a) Tang, K.; Ni, Z.; Liu, Q.; Quhe, R.; Zheng, Q.; Zheng, J.; Fei, R.; Gao, Z.; Lu, J. *Eur. Phys. J. B* **2012**, *85*, 301. (b) Zheng, F.; Liu, Z.; Wu, J.; Duan, W.; Gu, B.-L. *Phys Rev. B* **2008**, *78*, 085423. (c) Zhang, Z.; Guo, W. *Phys. Rev. B* **2008**, *77*, 075403.
(22) Basch, H.; Cohen, R.; Ratner, M. A. *Nano Lett.* **2005**, *5*, 1668.